Article

Ternary Triazole-Based Organic−Inorganic Proton-Conducting Hybrids Based on Computational Models for HT-PEMFC Application

Towa Bunno, Keiichiro Maegawa, Mateusz Wlazło, Kazuhiro Hikima, Atsushi Nagai,* and Atsunori Matsuda*

Cite This: *ACS Omega* 2023, 8, 44172−44182
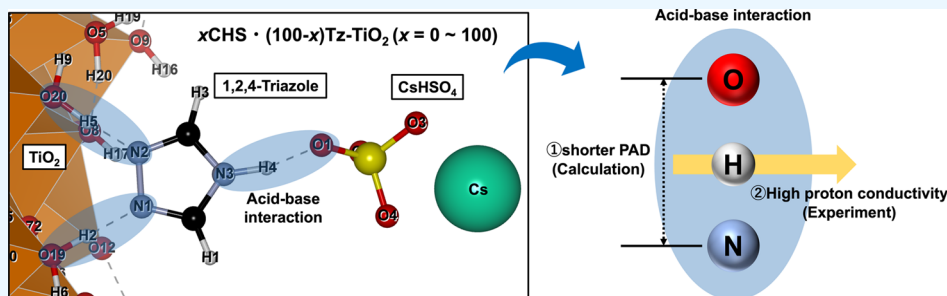
Read Online

ACCESS | Metrics & More | Article Recommendations | Supporting Information

ABSTRACT: We reported a new ternary hybrid anhydrous proton-conducting material based on triazole (Tz), wherein it interacted with TiO_2 and cesium hydrogen sulfate (CHS) constructed based on the acid−base interaction. It exhibited high proton conductivity derived by the two acid−base interactions: between CHS and Tz and between Tz and TiO_2. As a starting point of discussion, we attempted to theoretically predict the high/low proton conductivity using the push−pull protonated atomic distance (PAD) law, which makes it possible to predict the proton conductivity in the acid−base part based on density functional theory. The calculations indicate the possibility of achieving higher proton conductivity in the ternary composites (CHS·Tz−TiO_2) involving two acid−base interactions than in binary hybrids, such as CHS·Tz and TiO_2−Tz composites, suggesting the positive effect of two simultaneous acid−base interactions for achieving high proton conductivity. This result is supported by the experimental result with respect to synthesized materials obtained using the mechanochemical method. Adding TiO_2 to the CHS·Tz system causes a change in the CHS·Tz interaction and promotes proton dissociation, producing a new and fast proton-conducting layer through the formation of Tz−TiO_2 interaction. Applying CHS·Tz−TiO_2 to high-temperature proton exchange membrane fuel cells results in improved membrane conductivity and power-generation properties at 150 °C under anhydrous conditions.

INTRODUCTION

Herein, we report a new ternary hybrid anhydrous high proton-conducting material constructed based on the acid−base interaction. The first reported ternary composites based on triazole (Tz), wherein they interacted with TiO_2 and cesium hydrogen sulfate (CHS), exhibited high proton conductivity derived by the two simultaneous acid−base interactions: between CHS and Tz and between Tz and TiO_2. This study was conducted from a starting point of theoretical calculation using the density functional theory (DFT), according to our recently reported method "push−pull protonated atomic distance (PAD) effect" that enables prediction of the proton conductivity in each moiety of acid−base interactions. The experimentally synthesized ternary composites of CHS·Tz−TiO_2 exhibited a high proton conductivity that can support the theoretical calculation result.

Organic materials coordinated using an acid or a base, called "organic salts", which are structured based on an acid−base interaction, have been receiving considerable research attention owing to their high-temperature anhydrous proton conductivity.[1−5] Organic salt-based proton conductors are commonly based on the heterocyclic five- or six-membered ring compounds containing one or more nitrogen atoms.[6,7] The base site of them reacts with and anchors the acid in the system, resulting in stable and high proton conductivity even under anhydrous conditions.[8,9] Phosphoric acid (PA)-modified polybenzimidazole (PBI), which is characterized by the acid−base interaction between the imidazolium part of PBI and PA, is a representative organic salt exhibiting proton conductivity under high-temperature operations.[10−12] Various other organic salt materials have been investigated as proton conductors.[13] Kajita et al. studied H_2SO_4-swollen poly(4-vinylpyridine)
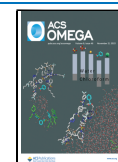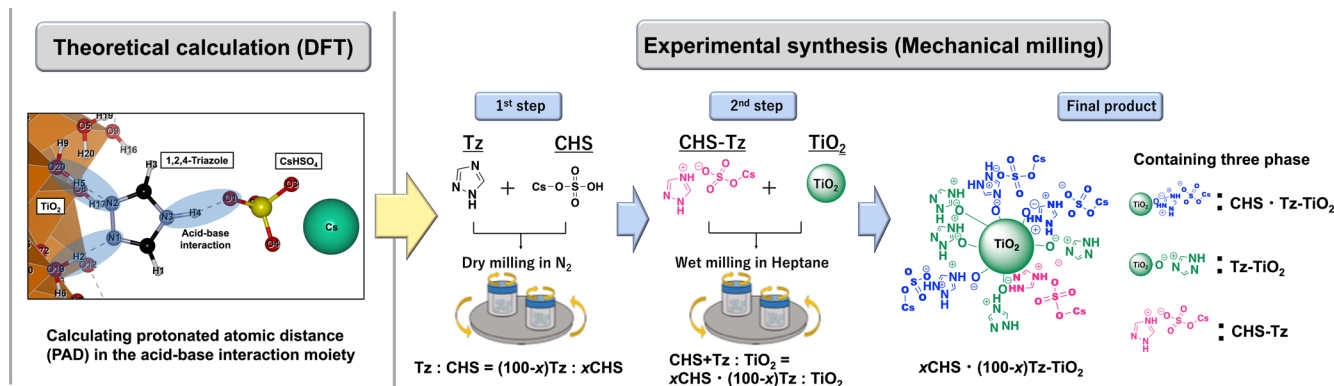
Figure 1. Procedure to develop proton-conducting inorganic—organic hybrids is based on computational models.

(PVP), which exhibited high proton conductivity.[14] Lee et al. studied quaternary ammonium (QA)-biphosphate ion-pair-coordinated polyphenylene (PA-doped QAPOH) derived based on high PA affinity and high tolerance of PA leaching, which shows high proton conductivity that remains stable over a wide temperature range.[15] Furthermore, Martinelli et al. reported a new proton conductor based on imidazolium that is hydrated using 12-tungstophosphate through an acid—base interaction.[16] We synthesized azole-based composites mixed with $CsHSO_4$ (CHS), an inorganic solid acid, using a mechanochemical method.[17,18] Forming acid—base interactions based on the new N—O bonding between azoles and CHS enables improved proton conductivity under a wide range of temperatures. $CsHSO_4$-1,2,4-triazole (CHS·Tz) shows the highest proton conductivity among several types of evaluated azoles, such as triazole, imidazole, benzoimidazole, and guanine. CHS·Tz is synthesized via an acid—base reaction, resulting in high proton conductivity over a wide range of temperatures by eliminating the superprotonic phase transition of pure CHS. However, the proton conductivity value achieved in CHS·Tz needs further improvement (1×10^{-3} S cm^{-1}). Thus, we hypothesize that Tz, which has two base sites, enables a reaction with extra protonic acid in addition to the CHS. We believe that the proton conductivity property of CHS·Tz can be improved by using different types of acids for the interaction with the remaining base sites in Tz. In the previous report, the proton conductivity of CHS-titanium dioxide (TiO_2) composites, as inorganic—inorganic proton conductors, eliminates phase transition of the proton conductivity.[17,19,20] Similarly, Ponomareva and Lavrova reported the influence of dispersed TiO_2 on the proton conductivity of CHS, which increased more than 2 orders of magnitude compared to that of pure CHS at low temperatures owing to the strong interface interaction between CHS and TiO_2 in the composites.[21]

Owing to these circumstances, in this study, we design a new proton-conducting hybrid formed via an acid—base interaction, in which two interactions occur: one between CHS and Tz and another between TiO_2 and Tz. Because of the two base sites (N) of Tz that can react with acids, the CHS·Tz—TiO_2 system requires Tz as the core, and the protons of the sulfate groups on CHS and the titanol groups (−OH) on the TiO_2 surface must bond through hydrogen bonds (Figure 1). Because of the two acid—base interactions, a ternary system with TiO_2 added to CHS·Tz is designed that is expected to achieve high proton conductivity under anhydrous conditions. As the starting point of design, the proton dissociativity and proton conductivity of

the designed material are predicted through molecular simulation using a molecular model of the designed material. Recently, we proposed a method for predicting the proton conductivity of organic salts, which is called the "push—pull PAD effect". We observed that when two or more materials are combined via hydrogen bonding based on an acid—base interaction, proton conductivity increases as the interatomic distance between the acid and base materials decreases.[22] Therefore, the model compounds, such as CHS·Tz, Tz—TiO_2, and CHS·Tz—TiO_2, are designed herein; the distance between the base and acid, called PAD, is calculated by using DFT to validate the proton conductivity of these salts. Experimental synthesis was then conducted to confirm the corroboration with the results of the DFT calculations. We synthesized the ternary hybrid nanoparticles (NPs) which are CHS·Tz—TiO_2 via a two-step method involving mechanochemical synthesis using high-energy planetary ball milling (Figure 1). Finally, the examined proton conductor is applied to the PA-doped PBI (PA—PBI),[23−26] the most popular electrolyte for high-temperature proton exchange membrane fuel cells (HT-PEMFCs) for evaluating HT-PEMFCs performance under 150 °C anhydrous conditions. Unlike the development of novel polymer membranes, which has been reported in many recent years, this is a simple method of compositing a proton conductor into a conventional PBI membrane.[27,28]

■ EXPERIMENTAL SECTION

Calculations. DFT calculations were performed using the planewave VASP code[29−32] with the Perdew—Burke—Ernzerhof functional[33] and the D3 dispersion correction[34,35] (DFT/PBE-D3(BJ) level of theory). For the final structural optimization, the planewave basis cutoff was set to 500 eV. The geometries of the model systems were relaxed until the maximum force component vanished below 0.05 eV/Å. The Pymatgen[36] Python library was used for the preparation of model structures and result analysis, and VESTA[37] was used for visualization.

Materials. Reagent grade $CsHSO_4$ (CHS) (Mitsuwa Chemical, 99%), 1,2,4-triazole($C_2H_3N_3$) (Tz) (FUJIFILM Wako Pure Chemical), and titanium oxide (TiO_2) (Sigma-Aldrich, P25) were used as starting materials for the synthesis of xCHS·(100-x)Tz—TiO_2 composites.

Synthesis of xCHS·(100-x)Tz and xCHS·(100-x)Tz—TiO_2. The mechanochemical synthesis of xCHS·(100-x)Tz was conducted for 2 h in a N_2 atmosphere using a planetary ball mill (pulverizette 7, Fritsch), an agate jar (45 mL), and agate balls (10 balls of ϕ10 mm in diameter); subsequently,
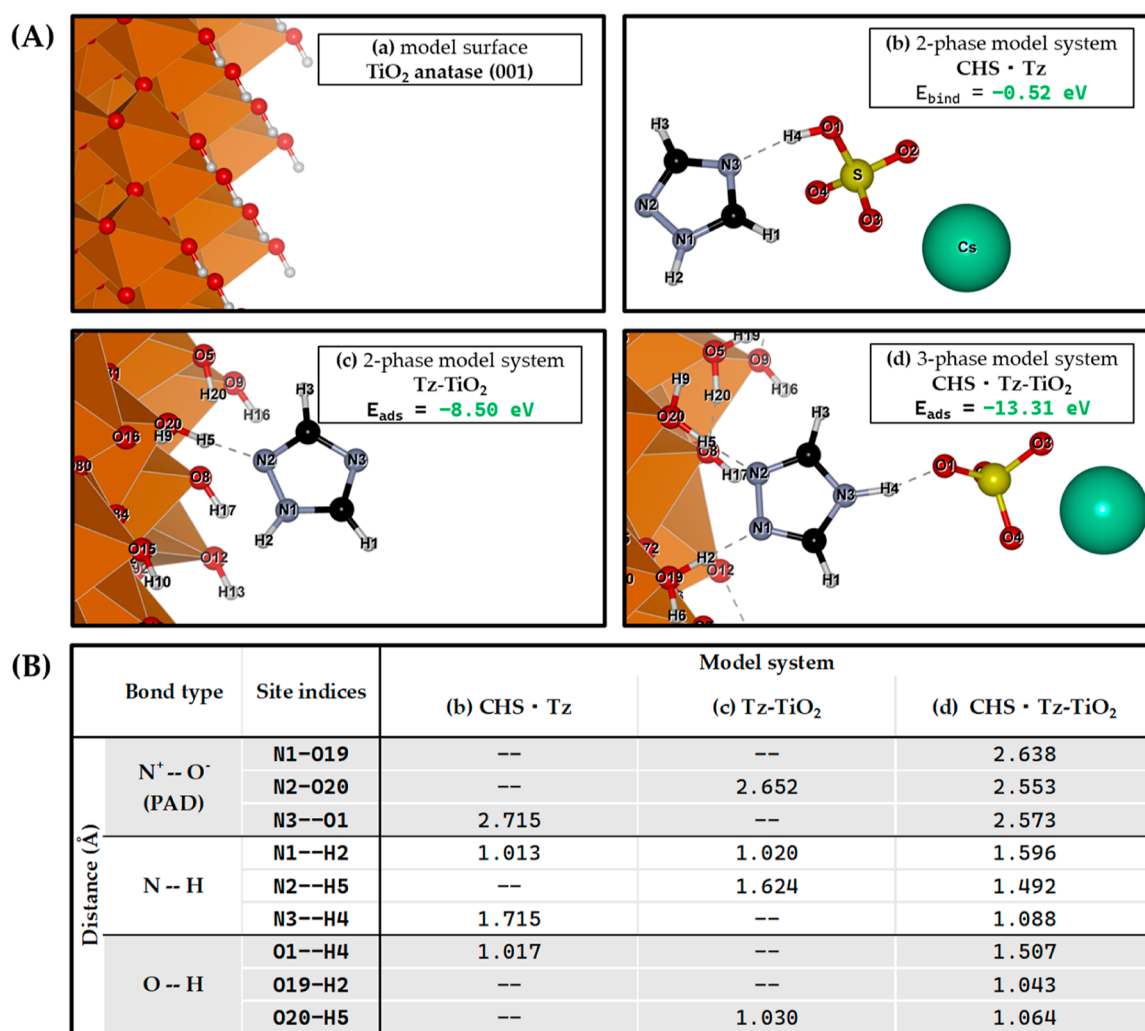
Figure 2. (A) Schematics of DFT-relaxed structures: (a) TiO_2 anatase (001) surface slab in vacuum (top left), (b) CHS·Tz compound (top right), (c) TiO_2 with an adsorbed Tz molecule (bottom left), and (d) TiO_2 with an adsorbed CHS·Tz compound (bottom right). The TiO_6 coordination polyhedra represent the TiO_2 surface, while the ball-and-stick model (oxygen/red, nitrogen/blue, carbon/black, hydrogen/white, sulfur/yellow, and cesium/teal) represents the surface hydroxyl groups and the adsorbed molecules. (B) Comparison of distances between N^+-O^-, N—H, and O—H in three model systems with DFT-relaxed geometries.

CHS and Tz with specific molar ratios were added. The rotation speeds of the milling jar and table were set to 720 rpm with a constant rotation ratio of 1:1. The composite ratio x (mol %) in xCHS·$(100-x)$Tz was varied between 0 and 100, with a fixed total sample weight of 2 g in the jar. After obtaining xCHS·$(100-x)$Tz, xCHS·$(100-x)$Tz−TiO_2 was prepared through wet mechanochemical treatment using heptane (Sigma-Aldrich) as the solvent in an Ar atmosphere. Subsequently, 1 g of as-synthesized xCHS·$(100-x)$Tz and 1 g of TiO_2 were mixed and added to the milling jar to realize a total weight of 2 g. The rotation speeds of the milling jar and table were set to 450 rpm with a constant rotation ratio of 1:1 for 1 h and a 10 min break, and then this 70 min process was repeated 12 times. The same apparatus used for the synthesis of xCHS·$(100-x)$Tz was used for the wet mechanochemical synthesis of xCHS·$(100-x)$Tz−TiO_2. Finally, 5 mL of heptane was added to the milling jar to realize wet ball milling.

Fabrication of PBI Composite Membranes. Preparation of the PBI composite membranes were conducted according to our previous studies.[38,39] The designed proton conductors (xCHS·$(100-x)$Tz or xCHS·$(100-x)$Tz−TiO_2) were added to

N,N-dimethylacetamide (DMAc) (FUJIFILM Wako Pure Chemical), and the obtained suspension was homogenized through sonication for 30 min. A commercial PBI (Sato Light Industrial, 10 wt % in DMAc) solution was added to the well-dispersed suspension to realize a diluted PBI (3 wt % in DMAc) solution containing the proton conductor. The PBI solution was sonicated for 30 min and stirred at 400 rpm for 1 h at room temperature (RT) to achieve a well-dispersed solution. This solution was cast onto a Petri dish (ϕ = 97 mm) and dried in an electric oven by gradually increasing the temperature from 30 to 120 °C. The thickness of the produced PBI electrolyte membrane is 50 μm. The proportion ratio of the prepared proton conductor in the PBI membrane was 2 wt %.

For evaluating the obtained membrane as a fuel cell, conducting power-generation tests, and measuring conductivity, 85% PA (FUJIFILM Wako Pure Chemical) was doped with a fixed amount (8 mol) according to the PA doping level (PADL) calculation, by controlling the immersion time in PA solution, for both pristine PBI and composite membrane. The formula for calculating PADL can be written as follows
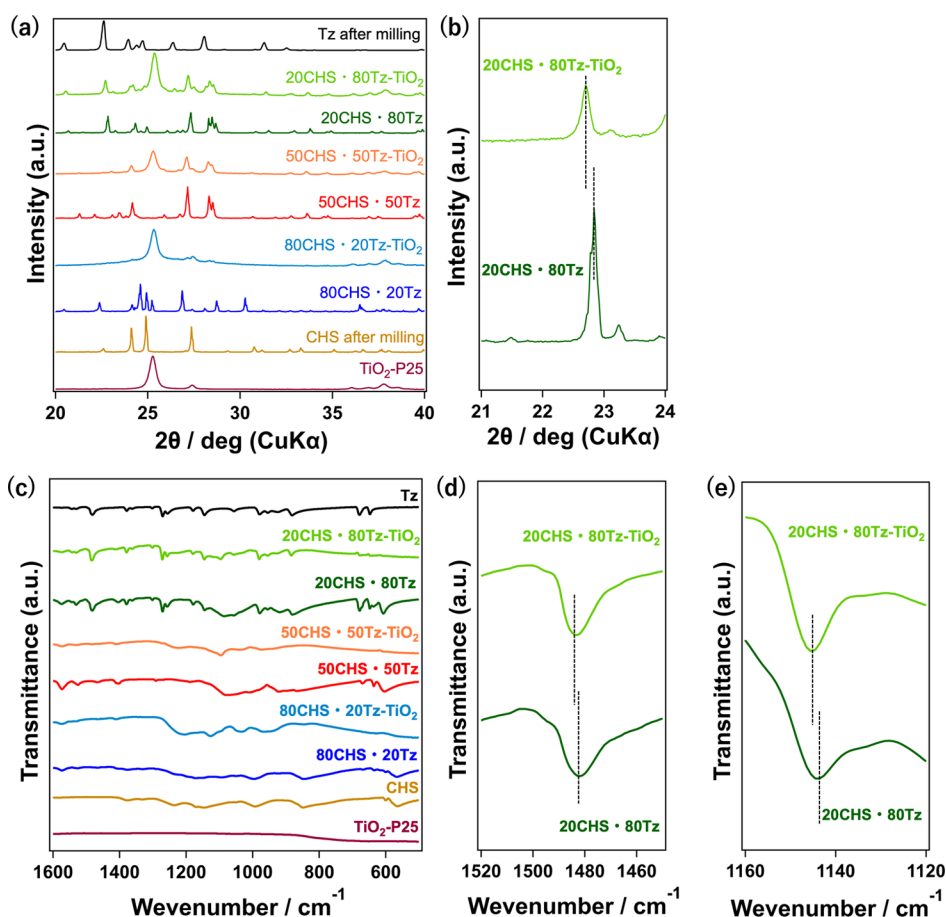
Figure 3. (a) XRD patterns of Tz, CHS, and TiO_2 (P25) as starting materials and of xCHS·(100-x)Tz with variable molar ratio x (x = 20, 50, and 80) synthesized by dry mechanochemical synthesis and xCHS (100-x)Tz−TiO_2 with variable molar ratio x (x = 20, 50, and 80) synthesized by wet mechanochemical synthesis. (b) Enlarged range of 2Θ = 21−24° for 20CHS·80Tz and 20CHS·80Tz−TiO_2. (c) FT-IR spectra of Tz, CHS, and TiO_2−P25 as starting materials, xCHS·(100-x)Tz with the variable of molar ratio x (x = 20, 50, and 80) synthesized by dry mechanochemical synthesis, and xCHS·(100-x)Tz−TiO_2 with the variable of molar ratio x (x = 20, 50, and 80) synthesized by wet mechanochemical synthesis. (d) Enlarged figure of FT-IR spectra at 1450−1520 cm^{-1} for 20CHS·80Tz and 20CHS·80Tz−TiO_2. (e) Enlarged figure of FT-IR spectra at 1120−1160 cm^{-1} for 20CHS·80Tz and 20CHS·80Tz−TiO_2.

$$PADL = 0.85 \times \left(\frac{W - W_0}{M_{PA}} \right) / \frac{W_0}{M_{PBI}}$$

where W_0 (g) and W (g) denote the weights of the PBI membrane before and after PA doping, respectively, M_{PA} is the molecular weight of PA (98 g/mol), M_{PBI} is the one-unit molecular weight of PBI (308 g/mol), and 0.85 is the PA ratio in the PA solution (in H_2O).

Structural Characterization. We observed the structural and morphological properties of the as-synthesized proton conductor and composite membranes via scanning electron microscopy (SEM) (S-4800, Hitachi), energy-dispersive X-ray spectroscopy (EDS) (Oxford UltimMax 40, Oxford Instruments), and optical microscopy (OLYMPUS). Powder X-ray diffraction (XRD) (Ultima IV, Rigaku, CuKα: 1.5418 Å) patterns were recorded to analyze the crystalline structure of the obtained proton conductors at RT. The changes in chemical structure were investigated using Fourier transform infrared spectroscopy (FT-IR; V-670 FT-IR, JASCO) with the attenuated total reflection method. Thermogravimetric-differential thermal analysis (Thermo Plus TG 8120, Rigaku) was used to evaluate the thermal stability of the prepared samples between RT and 800 °C, with a temperature increment rate of 5 °C min^{-1} using a Pt pan under an air atmosphere.

Impedance Spectroscopy Analysis. Proton conductivity at various temperatures was determined from AC impedance spectroscopy and measured with a frequency response analyzer (SP-300−2CH, BioLogic) from 7 MHz to 10 Hz. Powdered composites were sandwiched between Teflon-coated carbon paper (TGP-H-060H; Chemix) with 13 mm diameter and pressed in a stainless dye at 60 MPa for 10 min to be pelletized. The pellets were placed in the measurement cell with electrodes and then in a glass tube under the atmosphere with nitrogen gas feed at 250 mL min^{-1}. The temperature was controlled from RT to 150 °C by using a ribbon heater wrapped around the outer surface of the tube.

Intermediate-Temperature Fuel Cell Evaluation. The PA-doped PBI composite membrane and the catalyst coating electrodes (Pt/C:0.5 mg cm^{-2}; EC−10−05−7, ElectroChem) were sandwiched together by using a cell (JARI, Ex-1N) to form a membrane electrode assembly (MEA). To activate the proton conduction between the electrolyte membrane and the catalyst, we added a small drop of PA during MEA structuring.

The single cells were installed in a fuel cell characterization system (AutoPEM; TOYO Corp.) operated at 150 °C without humidification for 24 h. The cell temperature was monitored by inserting a thermocouple into the graphite block and kept constant using an attached heater. The anode and cathode

were supplied with hydrogen (H_2) and oxygen (O_2), respectively, at 100 mL min^{-1}.

RESULTS AND DISCUSSION

Before the synthesis of ternary hybrid NPs using Tz, CHS, and TiO_2 via ball milling, we designed and simulated the predictable structures of model salts, including CHS·Tz, Tz—TiO_2, and CHS·Tz—TiO_2 salts, based on acid—base interactions to decide the sequence of adding these salts during mechanical milling to produce high conductivity. Hence, we performed DFT calculations using the model compound, as shown in Figure 2.

The TiO_2 phase is modeled assuming the presence of an anatase polymorph, which is more prominent than rutile by a ratio of 3:1 in the standard TiO_2—P25 material used in this study.[40] The dominant presence of anatase polymorphs was also corroborated via the measured XRD pattern depicted in Figure 3, which resembles the pure anatase pattern more closely than the rutile pattern.[41] A surface slab was created by stacking four Ti and O atomic layers along the (001) direction and replicating the unit cell to obtain a $4 \times 4 \times 1$ supercell. The slab must be nonpolar and symmetric with a vacuum width of 20 Å between periodic images to eliminate their spurious interactions. This approach resulted in a total cell length of 37.5 Å along the direction perpendicular to the slab. The prepared surface was fully hydroxylated by decorating every topmost Ti site with an —OH group.

During the structural relaxation of the slab in a vacuum, the surface hydroxyl groups each remain oriented in the same direction, and no surface rearrangement occurs through surface H_2O formation nor otherwise. Upon introduction of the Tz molecule, a single hydrogen bond is formed with a surface OH group of TiO_2. The adsorption of the Tz molecule results in a small reorganization of the neighboring OH groups. Notably, although the Tz molecule is introduced in the 1H-1,2,4 configuration with two hydrogen atoms facing the surface, neither hydrogen is chemisorbed at the surface.

Examining the decrease in energy with respect to each system owing to adsorption is displayed next to each schematic in Figure 2A. This decrease in energy indicates a high level of surface rearrangement. The binding energy of CHS·Tz is relatively low (−0.52 eV) compared to the adsorption energies of Tz (−8.50 eV) and CHS·Tz (−13.31 eV) on TiO_2. This difference is, in large part, due to the formation of H_2O by rearrangement of surface OH groups caused, in the case of the three-phase hybrid, by excess protons introduced from the Tz fragment. This is only possible due to the proton hopping from CHS to the Tz fragment causing a cascade hopping effect of multiple protons.

In the case of the Tz—CHS fragment, the surface OH groups undergo significant reorganization. An additional OH group in the CHS moiety allows for a transformation from the 1H-1,2,4 to the 4H-1,2,4 configuration of triazole, while the two covalently bonded protons hop to the surface hydroxyl groups. In the neighborhood of the adsorption site, more rearrangement occurs in a cascade effect originating from the excess protons introduced by the CHS fragment. Notably, such rearrangement leaves an unsaturated bond in the CHS moiety, allowing the N—O bond formation, which has been proven essential for the excellent proton conductivity of CHS·Tz compounds.[20] To allow for this configuration in a hybrid system with TiO_2, we use the Tz molecule as the essential component, acting as the proton donor for the TiO_2 surface

and the proton acceptor for CHS. Therefore, the formation of this proton conduction channel must be possible in samples with a sufficiently high content of the Tz phase.

These resulting structures (presented schematically in Figure 2A) also show that forming a surface chemically bound with water is essential for the high proton conductivity of the three-phase CHS·Tz—TiO_2 system. This result is confirmed after the subsequent fabrication of the samples and measurement of the proton conductivity (Figure 5a). This theoretically proposed
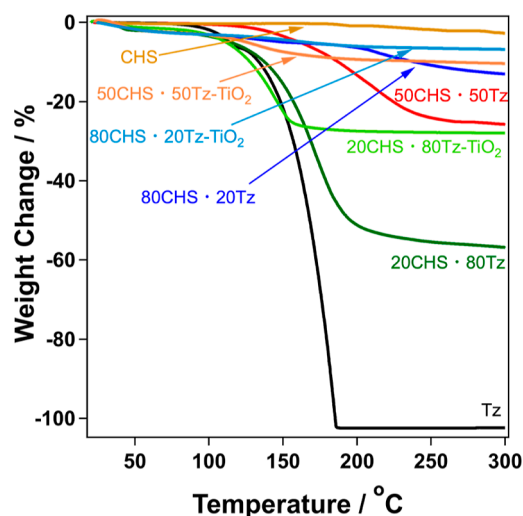

Figure 4. TGA of Tz, CHS, and TiO_2—P25 as starting materials, xCHS·(100-x)Tz with variable molar ratio x (x = 20, 50, and 80) synthesized by dry mechanochemical synthesis, and xCHS·(100-x)Tz—TiO_2 with variable molar ratio x (x = 20, 50, and 80) synthesized by wet mechanochemical synthesis.

proton conduction mechanism, corroborated by our previous study of two-phase CHS·Tz, can limit the temperature range in three-phase CHS·Tz—TiO_2. Such a limit is linked to the surface stability of water on TiO_2. According to thermogravimetric studies of titanium oxide powders (including P25), physiosorbed water is mainly removed up to 120 °C.[42] Above this temperature, the removal of chemisorbed water begins, deteriorating the presently discussed conduction pathway.

The computational results can also be discussed in terms of PAD, for which the general theoretical rule follows our recent report.[22] The PAD based on the amino group at the four positions in the 1,2,4-triazole ring (N3 in Figure 2A) is smaller on the order of CHS·Tz (2.715 Å) > CHS·Tz—TiO_2 (2.573 Å). Thus, TiO_2 modification supports the distance shortening and enables proton conduction with a lower energy barrier. On the other side of the molecule, sites 1—2 (N1 and N2 in Figure 2A, respectively) interact directly with the TiO_2 surface hydroxyl groups. In the case of Tz—TiO_2, N2 has a shorter ionic distance to a surface oxygen atom (2.652 Å) than that of CHS·Tz (2.715 Å) and CHS·Tz—TiO_2 (2.553 Å), while a second adsorption site forms at a similar distance (2.638 Å). This result combined with the aforementioned shortening of the N3 distance from O in the CHS moiety indicates the possibility of a high proton-conducting phase. Thus, CHS·Tz—TiO_2 appears as an organic—inorganic salt analogue of CHS·Tz and Tz—TiO_2. However, the PAD values differ due to the push—pull PAD effect.[43] From the PAD results, a donor of TiO_2 by doping or reacting donor or cation molecules increases the density of electrons of TiO_2 NPs.[44]
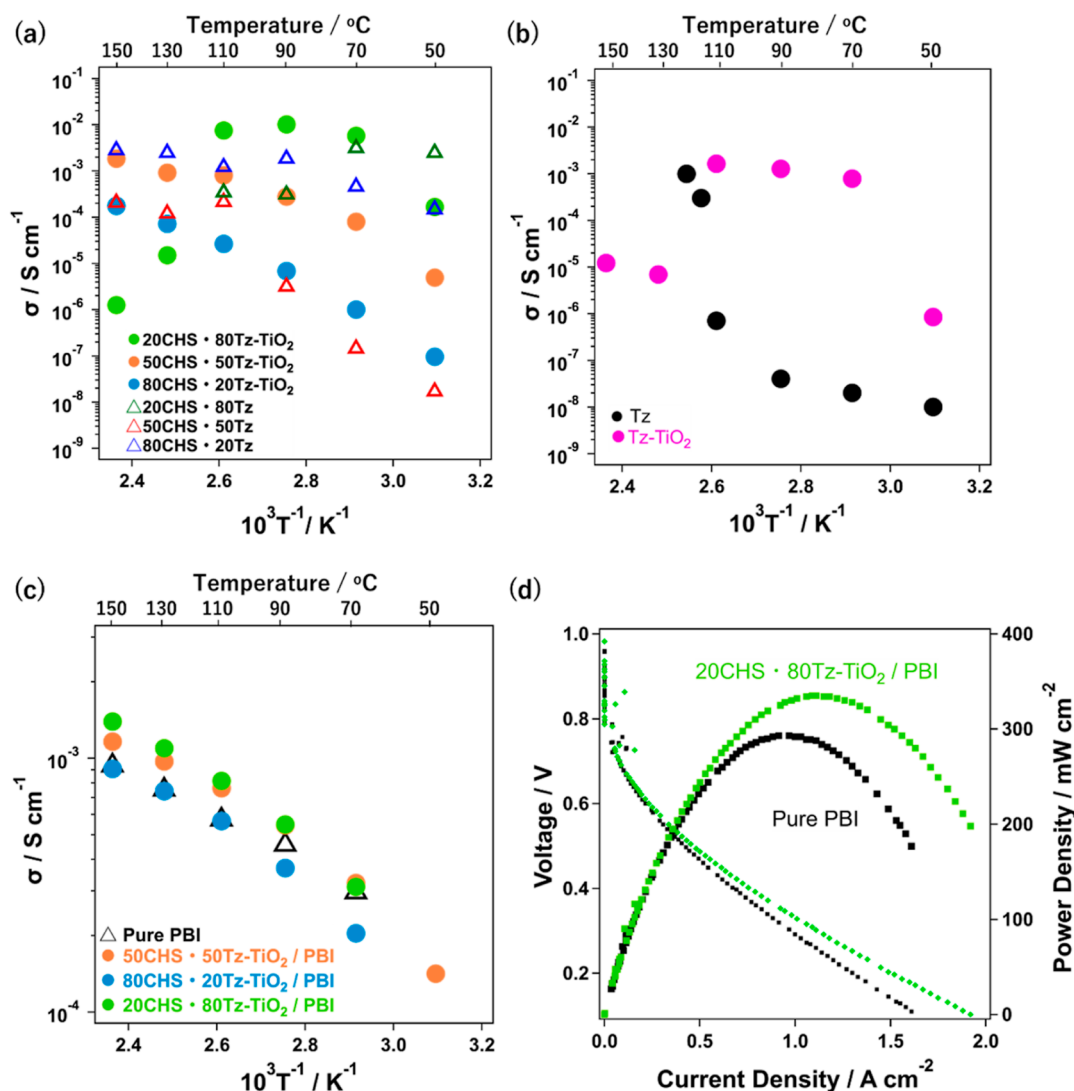
Figure 5. (a) Proton conductivity of xCHS·$(100-x)$Tz with variable molar ratio x (x = 20, 50, and 80) synthesized by dry mechanochemical synthesis and xCHS·$(100-x)$Tz−TiO$_2$ with variable molar ratio x (x = 20, 50, and 80) synthesized by wet mechanochemical synthesis. (b) Proton conductivity of Tz−TiO$_2$ (1:1) synthesized by wet mechanochemical synthesis. (c) Proton conductivity of pure/composite PBI membranes: pure PBI membrane doped with PA (PADL = 8) and PBI composite membrane containing 2 wt % of xCHS·$(100-x)$Tz−TiO$_2$ with a variable molar ratio of x (x = 20, 50, and 80) is synthesized via wet mechanochemical synthesis, doped with PA (PADL = 8) and measured for conductivity in the temperature range of 160−50 °C under a decreasing temperature scale in a dry N$_2$ atmosphere. (d) H$_2$/O$_2$ fuel cell performance with pure/composite PBI membranes: Pt/C (0.5 mg cm^{-2}), pure PBI membrane doped with PA (PADL = 8) (thickness = 50 μm), and PBI composite membrane containing 2 wt % of 20CHS·80Tz−TiO$_2$ synthesized via wet mechanochemical synthesis, doped with PA (PADL = 8) (thickness = 50 μm) at 150 °C at a rate of 100 mL min^{-1} H$_2$/O$_2$ for anode and cathode without operating backpressure.

In summary, based on these results, starting compounds, such as Tz, CHS, and TiO$_2$, were combined in a two-step ball milling: first, we carry out the mechanochemical synthesis of xCHS and $(100-x)$Tz with different contents (x = 20, 50, and 80) and then prepare the xCHS·$(100-x)$Tz as the binary mixtures and TiO$_2$ using the ball milling method (Figure 1).

The X-ray diffractograms of the starting materials and mechanochemically prepared xCHS·$(100-x)$Tz and xCHS·$(100-x)$Tz−TiO$_2$ with varied compositions are shown in Figure 3. Changes in the crystal structure of xCHS·$(100-x)$Tz using XRD have already been assigned and discussed in our previous paper.[17] As confirmed in a previous report, the crystalline structure changes by mixing CHS and Tz.[21] Generally, CHS shows three different crystalline phases (I, II, and III) depending on the temperature range.[45−49] The new peaks around 23.5−25° in CHS·Tz are the signals usually

observed in phases II and III of CHS under higher temperatures. This result indicates that CHS in CHS·Tz appears in the high-temperature crystalline phase associated with high proton conductivity even at RT.[50] By contrast, the prepared xCHS·$(100-x)$Tz−TiO$_2$ shows characteristic peaks attributed to those observed in xCHS·$(100-x)$Tz and TiO$_2$. The peaks at 25.5 and 27.5° corresponding to TiO$_2$[51] overlap on the diffraction patterns of xCHS·$(100-x)$Tz. Thus, no changes occur in the crystalline structure throughout the mechanical milling mixing between CHS·Tz and TiO$_2$ in the xCHS·$(100-x)$Tz and TiO$_2$ system. Meanwhile, in 20CHS·80Tz, a sample with a large amount of Tz, the most intensive peak of Tz at 23° shifted to a lower angle (Figure 3b). This shift was also observed for other peaks, suggesting that adding TiO$_2$ increases the spacing of the Tz crystal.

FT-IR spectra of the prepared xCHS·(100-x)Tz−TiO$_2$ are shown in Figure 3c,d. The FT-IR spectrum of CHS·Tz shows a characteristic peak for N−O in 1524 cm^{-1}, indicating the interaction between CHS and Tz caused by the mechanochemical method.[17] This interaction is also supported by the shift to lower wavenumbers in the signals attributed to OH modified by SO$_4$, which were identified at 848 and 1180 cm^{-1}. This finding shows that the acid−base interaction extends the distance of the OH bond in CHS.[52] Other peaks are attributed to the starting material. The strong absorption bands at 1280, 1180, 850, and 580 cm^{-1} were assigned to N=N in Tz, OH, OH in HSO$_4$, and SO$_4$, respectively.[53] The FT-IR spectra of xCHS·(100-x)Tz−TiO$_2$ can be correlated to the samples described earlier of xCHS·(100-x)Tz and TiO$_2$, indicating that chemical structural changes do not occur upon mechanochemical treatment. Meanwhile, Figure 3d,e shows that the C−N and N−H stretching bands at 1485 and 1145 cm^{-1} are shifted to higher wavenumbers, suggesting that OH groups on the TiO$_2$ surface protonate Tz by adding TiO$_2$.

To evaluate thermal stability before and after TiO$_2$ addition, we measure thermogravimetric analysis (TGA) for xCHS·(100-x)Tz and xCHS·(100-x)Tz−TiO$_2$, and the results are shown in Figure 4. Given that HT-PEMFC operates under high-temperature conditions above 100 °C (approximately 150 °C), the thermal stability of the electrolyte material requires evaluation. The weight losses from RT to approximately 100 °C result from adsorbed water on the surface of the complex.[54] The CHS weight shows a relatively small loss in this range and then decreases above 500 °C, indicating the material decomposition. In Tz, the weight losses appear above 120 °C, which is its melting point, and then it completely decomposes at 180 °C. By composing xCHS·(100-x)Tz, the remaining weight at 300 °C decreases as the Tz ratio increases. At 180 °C, where Tz decomposes completely, all composite samples show less weight losses than the amount of Tz based on its weight ratio; this result indicates improved thermal stability due to the chemical bonding with CHS·Tz (Table S1). Moreover, the start point of weight losses of Tz increases from 120 °C due to the chemical interaction with CHS.[18]

Adding TiO$_2$ through mechanical milling also affects the thermal stability. The TGA results show that xCHS·(100-x)Tz−TiO$_2$ are stable above 200 °C, while xCHS·(100-x)Tz begins to decrease in weight. As expected, samples with a high ratio of CHS show better stability regardless of whether with/without TiO$_2$. Furthermore, as with xCHS·(100-x)Tz, the weight loss of the Tz portion at 180 °C is suppressed in xCHS·(100-x)Tz−TiO$_2$ by complexation (Table S1). These results suggest that these proton conductors show feasible application to HT-PEMFC due to their thermal stability at 150 °C.

Figure 5a shows the temperature dependence of the proton conductivities of xCHS·(100-x)Tz and xCHS·(100-x)Tz−TiO$_2$ under dry air (N$_2$). Our previous literature shows that the proton conductivity of xCHS·(100-x)Tz improves as the value of x increases, showing the highest conductivity of 3×10^{-3} S cm^{-1} around 150 °C in 80CHS·20Tz,[17] and a similar value is obtained in this study. The nonlinear characteristics of the Tz-based compound in the Arrhenius plot are due to the phase transition behavior of Tz, which is well correlated to the previous research.[55] Several characteristic features are confirmed in the case of samples with TiO$_2$ addition. Adding TiO$_2$ improves the proton conductivity temperature dependence of 20CHS·80Tz and 50CHS·50Tz over the entire temperature range. In particular, 20CHS·80Tz−TiO$_2$ shows a maximum

proton conductivity of 1×10^{-2} S cm^{-1} in the specific temperature region between 90 and 110 °C. By comparison, the conductivity of 80CHS·20Tz−TiO$_2$ is lower than that of the composite without TiO$_2$ (80CHS·20Tz). The conductivity, especially in the case of a high molar ratio of Tz (x = 20), indicates the importance of the interaction between triazole and TiO$_2$. As reported by Martinelli et al., protonation of the surface of an inorganic material by an organic base material is considered the mechanism of the transforming proton transport.[16] The decrease in the proton conductivity of 80CHS·20Tz with the addition of TiO$_2$ is due to the incorporation of a proton insulator. Although the interaction causes the promotion of the proton conduction under the existence of free Tz, in this case TiO$_2$ addition contributes to decreasing the proton conduction when Tz reacts with CHS with the N−O interaction under a high CHS ratio.

To examine the interaction between Tz and TiO$_2$, we prepare model samples combined between pure Tz and TiO$_2$ with a mixing weight ratio of 1:1. Figure S1 shows the chemical structural evaluations using FT-IR. The conductivity of the fabricated Tz−TiO$_2$ (Figure 5b) shows that the phase transition temperature of the superprotonic phase observed in pure Tz[18] is shifted to the lower temperature. Interestingly, the maximum conductivity value in the high-temperature range (~110 °C) is not changed after the combination with TiO$_2$. By contrast, the phase transition that causes the rapid increase in proton conductivity occurs at relatively lower temperatures in Tz−TiO$_2$, compared with pristine Tz. This spread of the superprotonic phase indicates the acid−base interaction between the TiO$_2$ functional group and Tz.[16]

By summarizing the result of the proton conductivity measurements of the prepared samples, we can conclude that incorporating TiO$_2$ into the previously reported CHS·Tz contributes to the proton conductivity caused by the acid−base interaction; when combined, three effects of TiO$_2$ enhance the proton conductivity. First, it promotes proton dissociation and conduction in the CHS·Tz system by forming CHS·Tz−TiO$_2$. This finding is confirmed by the result that the PAD between the CHS and Tz becomes shorter after TiO$_2$ modification. Second, a high proton-conducting phase is formed by composing a Tz−TiO$_2$ system in the Tz excessive system, as confirmed by the shortest PAD between them. Lastly, as shown in the theoretical analysis, the excess protonation of the surface of TiO$_2$ by introducing the CHS phase is essential for opening a channel of high proton conduction, which is associated with the N−O bond formation in CHS·Tz composites reported earlier. The existence of this channel explains the abrupt drop (20CHS·80Tz−TiO$_2$) or stabilization (50CHS·50Tz−TiO$_2$), instead of a further increase, of proton conductivity between 110 and 130 °C. Amid this range, the temperature of 120 °C is previously reported as the onset of the removal of chemisorbed surface water from titanium oxide powders.[42] The high proton conductivity of the three-phase hybrid CHS·Tz−TiO$_2$ is achieved via the three effects mentioned above. Hence, CHS·Tz−TiO$_2$'s higher proton conductivity than CHS·Tz and Tz−TiO$_2$ supports our conclusion.

Investigation of Composite Electrolyte Membranes with Composite Additives. *Morphological Characterization of the PBI Composite Membrane.* The SEM−EDS observed the surface morphology of the proton conductor-added PBI membrane, the membrane's cross-sectional view, and the proton conductor's dispersibility (Figure S3).

According to the data, the prepared composites xCHS·(100-x)Tz and xCHS·(100-x)Tz−TiO$_2$ are homogeneously dispersed in the PBI membrane.

Proton Conductivity Evaluation. The proton conductivity of pure PBI and solid proton conductor-incorporated electrolyte membranes is measured at various temperatures, and the measurement results are shown in Figure 5c.

The PBI membrane comprising the prepared composite material exhibits high conductivity, as shown in Figure 5c. Compared with pure PBI membranes, the membranes having TiO$_2$-containing composites show higher proton conductivity. The PBI membrane comprising 20CHS·80Tz−TiO$_2$ exhibits the highest proton conductivity of 1.65×10^{-3} S cm^{-1} at 160 °C. This high proton conductivity is achieved owing to the high proton conductivity ($>1 \times 10^{-2}$ S cm^{-1}) of 20CHS·80Tz−TiO$_2$. Under the same PADL, the proton conductivity of the PBI membrane increases owing to the enhancement in protonic concentration as a result of incorporating proton conductors in the membrane.[56] Furthermore, a highly efficient proton transport channel is formed in the case of 20CHS·80Tz−TiO$_2$. Although the proton conductivity of 20CHS·80Tz−TiO$_2$ cannot be measured accurately at temperatures above 130 °C because of the melting of Tz, the addition of 20CHS·80Tz−TiO$_2$ to the PBI membrane allows the membrane to operate at temperatures >150 °C.

Fuel Cell Power-Generation Test. The composite membrane containing the prepared proton conductors characterized herein is evaluated as a medium-temperature, nonhumidified PEMFC to confirm its suitability for this operating condition. The key indicator to be achieved is to obtain high power density by the addition of a proton conductor, without changing the PADL.

Figure 5d shows the results of power-generation tests with respect to PBI electrolyte membranes containing 2 wt % of 20CHS·80Tz−TiO$_2$, which shows the highest proton conductivity over the entire range of temperatures. By the incorporation of 20CHS·80Tz−TiO$_2$, the maximum power density of the PBI membrane reached 335 mW cm^{-2}, which is higher than that of the pristine PBI membrane. Moreover, the maximum current density of the PBI membrane is 1.9 A cm^{-1}, which is higher than that of the PBI membrane. The slope of the I−V curve is moderated by adding 20CHS·80Tz−TiO$_2$. The bulk resistance of the fuel cell is calculated as the resistance of the electrolyte membrane using the slope of the I−V curve. The value of bulk resistance decreased from 0.36 to 0.31 Ω, indicating that the decreased resistance and increased proton conductivity of the electrolyte membrane result in the high power output. Adding 20CHS·80Tz−TiO$_2$ improves the properties of the fuel cell by increasing the proton conductivity of the PBI membrane. The electrochemical and fuel cell evaluations conducted herein confirmed that adding TiO$_2$ into the CHS·Tz proton conductor enhances its proton conductivity, especially in the case of the mixing molar ratio of $x = 20$ in xCHS·(100-x)Tz. The high proton conductivity of 20CHS·80Tz enhances the proton conductivity of the PBI membrane without changing the PADL, contributing to the enhancement of the fuel cell performance.

CONCLUSIONS

Based on the push−pull PAD theory and the previously determined high proton conduction channel in Tz−CHS, we predict the high or low proton conductivity of the Tz-based ternary material synthesized based on acid−base interactions.

According to the push−pull PAD theory, high proton conductivity is achieved when the PAD is shorter. As determined by DFT calculations, the PAD between CHS and Tz decreases when TiO$_2$ is added to CHS·Tz, indicating the promotion of proton dissociation between CHS and Tz. Additionally, the presence of Tz−CHS clearly shows the rearrangement of hydroxyl groups on the surface of TiO$_2$ into H$_2$O. This leads to the creation of an unsaturated bond in the CHS moiety via proton hopping and the possibility of N−O covalent bond formation between Tz and CHS, which is an important building block in realizing a high proton-conducting channel. A strong relationship between the DFT simulation and experimental data is observed in the case of mechanochemically synthesized xCHS·(100-x)Tz−TiO$_2$ having a variable molar ratio x ($x = 20$, 50, and 80). Incorporating TiO$_2$ into CHS·Tz changes its proton conductivity, especially in samples with a large Tz content, which exhibit high proton conductivity. Among the two- and three-phase samples with different mixing ratios, 20CHS·80Tz−TiO$_2$ shows the highest proton conductivity (1×10^{-2} S cm^{-1}). The Tz−TiO$_2$ sample shows higher conductivity than the Tz sample, experimentally confirming the theoretically derived interaction between Tz and TiO$_2$ and confirming the realization of a high proton-conducting channel. These results indicate that the CHS·Tz−TiO$_2$ system, wherein CHS·Tz and Tz−TiO$_2$ are mixed, may promote proton dissociation in CHS·Tz and the formation of efficient proton-conducting channels. These results show that the proposed push−pull PAD theory can also be used to determine the proton conductivity of Tz-based ternary proton-conducting salts. We demonstrate that PAD is correlated to conductivity, even in materials synthesized using the mechanical milling method. Herein, we also evaluate the performance of the PA-doped PBI membrane. The membrane containing the prepared 20CHS·80Tz−TiO$_2$ shows improved proton conductivity and high power density with respect to the PEMFC performance. For the organic salts, the proton shared with the acid and base plays an important role in proton conduction. Thus, organic salts are promising candidates as proton conductors for application in PEMFCs operating under anhydrous conditions. Developing electrode ionomers, including electrolytes, is still underway to realize the operation of fuel cells under medium temperatures and anhydrous conditions. Therefore, the discussion on the proton conductivity of organic salts based on acid−base interactions and the results of their fuel cell applications serve as a foundation to accelerate the future development of proton conductors under medium temperature and anhydrous conditions.

■ ASSOCIATED CONTENT

Ⓢ **Supporting Information**

The Supporting Information is available free of charge at https://pubs.acs.org/doi/10.1021/acsomega.3c06587.

FT-IR analysis and weight loss data obtained by TGA, SEM, and computed structures (PDF)

■ AUTHOR INFORMATION

Corresponding Authors

Atsushi Nagai − *Next-Generation Energy Systems Group, Centre of Excellence ENSEMBLE3 sp. z o.o., Warsaw 01-919, Poland;* ⓞ orcid.org/0000-0002-5871-1775; Email: atsushi.nagai@ensemble3.eu

Atsunori Matsuda − *Department of Electrical and Electronic Information Engineering, Toyohashi University of Technology, Toyohashi, Aichi 441-8580, Japan;* ⬤ orcid.org/0000-0002-6493-1205; Email: matsuda@ ee.tut.ac.jp

Authors

Towa Bunno − *Department of Electrical and Electronic Information Engineering, Toyohashi University of Technology, Toyohashi, Aichi 441-8580, Japan*

Keiichiro Maegawa − *Department of Electrical and Electronic Information Engineering, Toyohashi University of Technology, Toyohashi, Aichi 441-8580, Japan; Next-Generation Energy Systems Group, Centre of Excellence ENSEMBLE3 sp. z o.o., Warsaw 01-919, Poland;* ⬤ orcid.org/0000-0002-2547-3395

Mateusz Wlazło − *Next-Generation Energy Systems Group, Centre of Excellence ENSEMBLE3 sp. z o.o., Warsaw 01-919, Poland;* ⬤ orcid.org/0000-0001-5493-3154

Kazuhiro Hikima − *Department of Electrical and Electronic Information Engineering, Toyohashi University of Technology, Toyohashi, Aichi 441-8580, Japan;* ⬤ orcid.org/0000-0001-5714-4652

Complete contact information is available at:
https://pubs.acs.org/10.1021/acsomega.3c06587

Author Contributions

T.B. and K.M. contributed equally to this work. Towa Bunno led in the synthesis, analysis, data processing, and writing of this manuscript. Keiichiro Maegawa led the structuring of the concept of this research, planning, discussion, and writing of the manuscript. The above authors contributed equally in this study. Mateusz Wlazo led the computational study, designed the simulation model, and performed the calculations, including analyzing, interpreting, and describing the model results. He similarly contributed to the discussion on linking theoretical and experimental results. Kazuhiro Hikima prepared a comprehensive discussion of this work and helped establish the analysis method. Atsushi Nagai supervised the method application and the discussion of computational simulation and helped establish the concept of this manuscript. Atsunori Matsuda provided comprehensive support by acquiring research funding to establish the concept, experimentation, discussion, and writing. All authors provided comments on the manuscript and have reviewed and approved the manuscript that has not been accepted or published elsewhere.

Notes

The authors declare no competing financial interest.

■ REFERENCES

(1) Pu, H.; Ye, S.; Wan, D. Anhydrous proton conductivity of acid doped vinyltriazole-based polymers. *Electrochim. Acta* **2007**, *52* (19), 5879−5883.

(2) Rusanov, A. L.; Likhatchev, D.; Kostoglodov, P. V.; Müllen, K.; Klapper, M.; Schmidt, M. Proton-Exchanging Electrolyte Membranes Based on Aromatic Condensation Polymers. *Inorganic Polymeric Nanocomposites and Membranes*; Advances in Polymer Science, 2005; Vol. *179*, pp 83−134.

(3) Chen, J.; Cao, J.; Zhang, R.; Zhou, J.; Wang, S.; Liu, X.; Zhang, T.; Tao, X.; Zhang, Y. Modifications on Promoting the Proton Conductivity of Polybenzimidazole-Based Polymer Electrolyte Membranes in Fuel Cells. *Membranes* **2021**, *11* (11), 826−848.

(4) Rikukawa, M.; Sanui, K. Proton-conducting polymer electrolyte membranes based on hydrocarbon polymers. *Prog. Polym. Sci.* **2000**, *25* (10), 1463−1502.

(5) Sahoo, R.; Mondal, S.; Pal, S. C.; Mukherjee, D.; Das, M. C. Covalent-Organic Frameworks (COFs) as Proton Conductors. *Adv. Energy Mater.* **2021**, *11* (39), 2102300.

(6) Çelik, S. Ü.; Coşgun, S.; Akbey, Ü.; Bozkurt, A. Synthesis and proton conductivity studies of azole functional organic electrolytes. *Ionics* **2012**, *18* (1−2), 101−107.

(7) Jang, J.; Kim, D.-H.; Min, C.-M.; Pak, C.; Lee, J.-S. Azole structures influence fuel cell performance of phosphoric acid-doped poly(phenylene oxide) with azoles on side chains. *J. Membr. Sci.* **2020**, *605*, 118096.

(8) Liu, Y.; Yu, Q.; Yuan, J.; Ma, L.; Wu, Y. Brønsted acid−base polymer electrolyte membrane based on sulfonated poly(phenylene oxide) and imidazole. *Eur. Polym. J.* **2006**, *42* (9), 2199−2203.

(9) Farrokhi, M.; Abdollahi, M. Enhancing medium/high temperature proton conductivity of poly(benzimidazole)-based proton exchange membrane via blending with poly(vinyl imidazole-co-vinyl phosphonic acid) copolymer: Proton conductivity-copolymer microstructure relationship. *Eur. Polym. J.* **2020**, *131*, 109691.

(10) Asensio, J. A.; Sanchez, E. M.; Gomez-Romero, P. Proton-conducting membranes based on benzimidazole polymers for high-temperature PEM fuel cells. A chemical quest. *Chem. Soc. Rev.* **2010**, *39* (8), 3210−3239.

(11) Araya, S. S.; Zhou, F.; Liso, V.; Sahlin, S. L.; Vang, J. R.; Thomas, S.; Gao, X.; Jeppesen, C.; Kær, S. K. A comprehensive review of PBI-based high temperature PEM fuel cells. *Int. J. Hydrogen Energy* **2016**, *41* (46), 21310−21344.

(12) Escorihuela, J.; Olvera-Mancilla, J.; Alexandrova, L.; Del Castillo, L. F.; Compan, V. Recent Progress in the Development of Composite Membranes Based on Polybenzimidazole for High Temperature Proton Exchange Membrane (PEM) Fuel Cell Applications. *Polymers* **2020**, *12* (9), 1861.

(13) Atanasov, V.; Lee, A. S.; Park, E. J.; Maurya, S.; Baca, E. D.; Fujimoto, C.; Hibbs, M.; Matanovic, I.; Kerres, J.; Kim, Y. S. Synergistically integrated phosphonated poly(pentafluorostyrene) for fuel cells. *Nat. Mater.* **2021**, *20* (3), 370−377.

(14) Kajita, T.; Tanaka, H.; Noro, A.; Matsushita, Y.; Nakamura, N. Acidic liquid-swollen polymer membranes exhibiting anhydrous proton conductivity higher than 100 mS cm^{-1} at around 100. *J. Mater. Chem. A* **2019**, *7* (26), 15585−15592.

(15) Lee, K.-S.; Spendelow, J. S.; Choe, Y.-K.; Fujimoto, C.; Kim, Y. S. An operationally flexible fuel cell based on quaternary ammonium-biphosphate ion pairs. *Nat. Energy* **2016**, *1* (9), 16120−16127.

(16) Martinelli, A.; Otero-Mato, J. M.; Garaga, M. N.; Elamin, K.; Rahman, S. M. H.; Zwanziger, J. W.; Werner-Zwanziger, U.; Varela, L. M. A New Solid-State Proton Conductor: The Salt Hydrate Based on Imidazolium and 12-Tungstophosphate. *J. Am. Chem. Soc.* **2021**, *143* (34), 13895−13907.

(17) Oh, S.-y.; Kawamura, G.; Muto, H.; Matsuda, A. Anhydrous protic conduction of mechanochemically synthesized CsHSO4-Azole-derived composites. *Electrochim. Acta* **2012**, *75*, 11−19.

(18) Aili, D.; Gao, Y.; Han, J.; Li, Q. Acid-base chemistry and proton conductivity of CsHSO$_4$, CsH$_2$PO$_4$ and their mixtures with N-heterocycles. *Solid State Ionics* **2017**, *306*, 13−19.

(19) Oh, S.-y.; Kawamura, G.; Muto, H.; Matsuda, A. Mechanochemical synthesis of proton conductive composites derived from cesium dihydrogen phosphate and guanine. *Solid State Ionics* **2012**, *225*, 223−227.

(20) Oh, S.-Y.; Yoshida, T.; Kawamura, G.; Muto, H.; Matsuda, A. Solid-state mechanochemical synthesis of CsHSO$_4$ and 1,2,4-triazole inorganic-organic composite electrolytes for dry fuel cells. *Electrochim. Acta* **2011**, *56* (5), 2364−2371.

(21) Ponomareva, V. G.; Lavrova, G. V. The investigation of disordered phases in nanocomposite proton electrolytes based on MeHSO4 (Me = Rb, Cs, K). *Solid State Ionics* **2001**, *145* (1−4), 197−204.

(22) Maegawa, K.; Bunno, T.; Yokoyama, I.; Nagai, A.; Matsuda, A. Theoretical Calculations of Organic Salts and Their Correlation with Proton Conductivity. *ACS Appl. Polym. Mater.* **2023**, *5* (5), 3405−3415.

(23) Li, Q.; Jensen, J. O.; Savinell, R. F.; Bjerrum, N. J. High temperature proton exchange membranes based on polybenzimidazoles for fuel cells. *Prog. Polym. Sci.* **2009**, *34* (5), 449−477.

(24) Li, Q.; He, R.; Jensen, J. O.; Bjerrum, N. J. PBI-Based Polymer Membranes for High Temperature Fuel Cells- Preparation, Characterization and Fuel Cell Demonstration. *Fuel Cells* **2004**, *4* (3), 147−159.

(25) Savadogo, O. Emerging membranes for electrochemical systems. *J. Power Sources* **2004**, *127* (1−2), 135−161.

(26) Chandan, A.; Hattenberger, M.; El-kharouf, A.; Du, S.; Dhir, A.; Self, V.; Pollet, B. G.; Ingram, A.; Bujalski, W. High temperature (HT) polymer electrolyte membrane fuel cells (PEMFC) - A review. *J. Power Sources* **2013**, *231*, 264−278.

(27) Li, X.; Ma, H.; Wang, P.; Liu, Z.; Peng, J.; Hu, W.; Jiang, Z.; Liu, B.; Guiver, M. D. Highly Conductive and Mechanically Stable Imidazole-Rich Cross-Linked Networks for High-Temperature Proton Exchange Membrane Fuel Cells. *Chem. Mater.* **2020**, *32* (3), 1182−1191.

(28) Wang, P.; Li, X.; Liu, Z.; Peng, J.; Shi, C.; Li, T.; Yang, J.; Shan, C.; Hu, W.; Liu, B. Construction of highly conductive PBI-based alloy membranes by incorporating PIMs with optimized molecular weights for high-temperature proton exchange membrane fuel cells. *J. Membr. Sci.* **2022**, *659*, 120790.

(29) Kresse, G.; Hafner, J. Ab initio molecular dynamics for liquid metals. *Phys. Rev. B: Condens. Matter Mater. Phys.* **1993**, *47* (1), 558−561.

(30) Kresse, G.; Hafner, J. Ab initio molecular-dynamics simulation of the liquid-metal-amorphous-semiconductor transition in germanium. *Phys. Rev. B: Condens. Matter.* **1994**, *49* (20), 14251−14269.

(31) Kresse, G.; Furthmüller, J. Efficiency of ab-initio total energy calculations for metals and semiconductors using a plane-wave basis set. *Comput. Mater. Sci.* **1996**, *6* (1), 15−50.

(32) Kresse, G.; Furthmuller, J. Efficient iterative schemes for ab initio total-energy calculations using a plane-wave basis set. *Phys. Rev. B: Condens. Matter.* **1996**, *54* (16), 11169−11186.

(33) Perdew, J. P.; Burke, K.; Ernzerhof, M. Generalized Gradient Approximation Made Simple. *Phys. Rev. Lett.* **1996**, *77* (18), 3865−3868.

(34) Grimme, S.; Antony, J.; Ehrlich, S.; Krieg, H. A consistent and accurate ab initio parametrization of density functional dispersion correction (DFT-D) for the 94 elements H-Pu. *J. Chem. Phys.* **2010**, *132* (15), 154104.

(35) Grimme, S.; Ehrlich, S.; Goerigk, L. Effect of the damping function in dispersion corrected density functional theory. *J. Comput. Chem.* **2011**, *32* (7), 1456−1465.

(36) Ong, S. P.; Richards, W. D.; Jain, A.; Hautier, G.; Kocher, M.; Cholia, S.; Gunter, D.; Chevrier, V. L.; Persson, K. A.; Ceder, G. Python Materials Genomics (pymatgen): A robust, open-source python library for materials analysis. *Comput. Mater. Sci.* **2013**, *68*, 314−319.

(37) Momma, K.; Izumi, F. VESTA 3 for three-dimensional visualization of crystal, volumetric and morphology data. *J. Appl. Crystallogr.* **2011**, *44* (6), 1272−1276.

(38) Maegawa, K.; Nagai, H.; Kumar, R.; Abdel-Galeil, M. M.; Tan, W. K.; Matsuda, A. Development of polybenzimidazole modification with open-edges/porous-reduced graphene oxide composite membranes for excellent stability and improved PEM fuel cell performance. *J. Chem. Phys.* **2023**, *294*, 126994.

(39) Ooi, Y. X.; Ya, K. Z.; Maegawa, K.; Tan, W. K.; Kawamura, G.; Muto, H.; Matsuda, A. Incorporation of titanium pyrophosphate in polybenzimidazole membrane for medium temperature dry PEFC application. *Solid State Ionics* **2020**, *344*, 115140.

(40) Ohno, T.; Sarukawa, K.; Tokieda, K.; Matsumura, M. Morphology of a TiO$_2$ Photocatalyst (Degussa, P-25) Consisting of Anatase and Rutile Crystalline Phases. *J. Catal.* **2001**, *203* (1), 82−86.

(41) Hanaor, D. A. H.; Sorrell, C. C. Review of the anatase to rutile phase transformation. *J. Mater. Sci.* **2011**, *46* (4), 855−874.

(42) Mueller, R.; Kammler, H. K.; Wegner, K.; Pratsinis, S. E. OH Surface Density of SiO$_2$ and TiO$_2$ by Thermogravimetric Analysis. *Langmuir* **2003**, *19* (1), 160−165.

(43) Ponomareva, V. G.; Lavrova, G. V. Influence of dispersed TiO$_2$ on protonic conductivity of CsHSO$_4$. *Solid State Ionics* **1998**, *106* (1−2), 137−141.

(44) Amano, F.; Tosaki, R.; Sato, K.; Higuchi, Y. Effects of donor doping and acceptor doping on rutile TiO$_2$ particles for photocatalytic O$_2$ evolution by water oxidation. *J. Solid State Chem.* **2018**, *258*, 79−85.

(45) Chisholm, C. R. I.; Jang, Y. H.; Haile, S. M.; Goddard, W. A. Superprotonic phase transition of CsHSO$_4$: A molecular dynamics simulation study. *Phys. Rev. B: Condens. Matter Mater. Phys.* **2005**, *72* (13), 134103.

(46) Belushkin, A. P-T phase diagram of CsHSO$_4$. Neutron scattering study of structure and dynamics. *Solid State Ionics* **1995**, *77*, 91−96.

(47) Chisholm, C. R. I.; Haile, S. M. X-ray structure refinement of CsHSO4 in phase II. *Mater. Res. Bull.* **2000**, *35* (7), 999−1005.

(48) Chisholm, C. Superprotonic behavior of Cs$_2$(HSO$_4$)(H2PO$_4$) - a new solid acid in the CsHSO$_4$-CsH$_2$PO$_4$ system. *Solid State Ionics* **2000**, *136−137* (1−2), 229−241.

(49) Mizuno, M. Proton dynamics in phase II of CsHSO$_4$ studied by ^{1}H NMR. *Solid State Ionics* **2004**, *167* (3−4), 317−323.

(50) Wang, S.; Otomo, J.; Ogura, M.; Wen, C.-j.; Nagamoto, H.; Takahashi, H. Preparation and characterization of proton-conducting CsHSO$_4$-SiO$_2$ nanocomposite electrolyte membranes. *Solid State Ionics* **2005**, *176* (7−8), 755−760.

(51) Janus, M.; Morawski, A. New method of improving photocatalytic activity of commercial Degussa P25 for azo dyes decomposition. *Appl. Catal., B* **2007**, *75* (1−2), 118−123.

(52) Oh, S. Y.; Yoshida, T.; Kawamura, G.; Muto, H.; Sakai, M.; Matsuda, A. Proton conductivity and fuel cell property of composite electrolyte consisting of Cs-substituted heteropoly acids and sulfonated poly(ether-ether ketone). *J. Power Sources* **2010**, *195* (18), 5822−5828.

(53) Baran, J.; Marchewka, M. K. Vibrational investigation of phase transitions in CsHSO$_4$ crystal. *J. Mol. Struct.* **2002**, *614* (1−3), 133−149.

(54) Saadatkhah, N.; Carillo Garcia, A.; Ackermann, S.; Leclerc, P.; Latifi, M.; Samih, S.; Patience, G. S.; Chaouki, J. Experimental methods in chemical engineering: Thermogravimetric analysis-TGA. *Can. J. Chem. Eng.* **2020**, *98* (1), 34−43.

(55) Pulst, M.; Balko, J.; Golitsyn, Y.; Reichert, D.; Busse, K.; Kressler, J. Proton conductivity and phase transitions in 1,2,3-triazole. *Phys. Chem. Chem. Phys.* **2016**, *18* (8), 6153−6163.

(56) Ooi, Y. X.; Ya, K. Z.; Maegawa, K.; Tan, W. K.; Kawamura, G.; Muto, H.; Matsuda, A. CHS-WSiA doped hexafluoropropylidene-containing polybenzimidazole composite membranes for medium temperature dry fuel cells. *Int. J. Hydrogen Energy* **2019**, *44* (60), 32201−32209.